DNS of Moderate-Temperature Gaseous Mixing Layers Laden with Multicomponent-Fuel Drops

Patrick C. Le Clercq[+*] and Josette Bellan[+,++†]
Jet Propulsion Laboratory[+]
California Institute of Technology[++]
Pasadena CA 91109-8099

A formulation representing multicomponent-fuel (MC-fuel) composition as a Probability Distribution Function (PDF) depending on the molar weight is used to construct a model of a large number of MC-fuel drops evaporating in a gas flow, so as to assess the extent of fuel specificity on the vapor composition. The PDF is a combination of two Gamma PDFs, which was previously shown to duplicate the behavior of a fuel composed of many species during single drop evaporation. The conservation equations are Eulerian for the flow and Lagrangian for the physical drops, all of which are individually followed. The gas conservation equations for mass, momentum, species and energy, are complemented by differential conservation equations for the first four moments of the gas-composition PDF; all coupled to the perfect gas equation of state. Source terms in all conservation equations couple the gas phase to the drops. The drop conservation equations for mass, position, momentum and energy are complemented by differential equations for four moments of the liquid-composition PDF. The simulations are performed for a three-dimensional mixing layer whose lower stream is initially laden with drops. Initial perturbations excite the layer to promote the double pairing of its four initial spanwise vortices to an ultimate vortex. The drop temperature is initially lower than that of the surrounding gas, initiating drop heating and evaporation. The results focus on both evolution and the state of the drops and gas when layers reach a momentum-thickness maximum past the double vortex pairing; particular emphasis is on the gas composition. Comparisons between simulations with n-decane, diesel and three kerosenes show that although at same initial Reynolds number and drop Stokes number distribution the growth and the rotational characteristics of the layers is unaffected by the fuel specificity, the global mixing is highly fuel specific. Analysis of the local conditions shows a high level of mixturre heterogeneity for all MC fuels and thus a single-component fuel cannot represent MC fuels. Substantial differences among the MC-fuel vapor composition can be traced to the original PDF representing the MC-fuel composition.

Introduction

The overwhelming majority of fuels used in spray combustion devices are complex mixtures of a myriad of chemical species; examples are diesel, gasoline and kerosene. The traditional way of modeling these fuels has been to consider the mixture as the sum of all its individual species[1,2] or as the sum of a solvent and a solute;[3] for obvious reasons, we call this the 'discrete' species approach (DSA). Due to computational overhead associated with a large number of species, complex fuels have so far not been simulated using the DSA. Ascertaining the role of different species in a complex fuel is, however, important during combustion because they have different impacts depending on the application. Recent developments in the modeling of multicomponent (MC) fuel drops have opened intriguing possibilities for modeling MC-fuel sprays[4–7] in a computationally efficient manner. These recent models are based on the well-established theory of Continuous Thermodynamics (CT),[8,9] in which the chemical potential for a mixture containing numerous components is appropriately represented, and the Gibbs function is derived through molecular thermodynamic methods in terms of the probability distribution function (PDF) describing the mixture composition. The concepts are fundamental and independent of the physicochemical model chosen for the chemical potential. Having specified an initial PDF, the evolution of the mixture is governed by thermodynamic relationships and/or conservation equations. Although the most general PDF will depend on many variables, it has been shown, with validation, that the single-Gamma PDF depending on the molar weight, m, can represent a homologous species class.[9–12]

Single-Gamma PDF models applied to drop evaporation[4–6] are, however, restricted to negligible fuel vapor in the drop-surrounding gas, as shown by Harstad et al.[7] A combination of two Gamma PDFs (DGPDF) as a function of m is necessary to capture the evaporation of drops in a gas containing substantial fuel vapor,[7] as in sprays. Moreover, Harstad and Bellan[13] have enlarged the DGPDF concept through appropriate thermodynamic modeling and shown that a sin-

*Post-Doctoral Scholar, AIAA Member.
†Senior Research Scientist, AIAA Associate Fellow (corresponding author, josette.bellan@jpl.nasa.gov).

gle DGPDF can represent several homologous species classes.

This study addresses the problem of MC-fuel drop evaporation in shear flows, such as in sprays, and inquires into the various aspcts of the flow with particular empahsis on the species distribution. All simulations are performed in the pre-transitional regime so as to uncouple the composition and turbulence features of the flow. The interest is here on exploring the influence that the MC aspect has on the flow/drop coupled interaction, both from the standpoint of the flow and the drop characteristics. Since the drop/flow interaction exists only as long as the drop has not entirely evaported, the interaction characteristic time is governed by the fuel identity, the initial drop size, the initial drop temperature, the initial gas composition and the initial gas temperature, particularly compared to the fuel boiling temperature. Thus, at same drop size and gas characteristics, single-species, also called singlecomponent (SC), fuel drop evaporation is governed by the single value of the fuel boiling temperature (at the specified pressure), while for MC-fuel drops the fuel boiling temperature continuously changes with composition as the drop evaporates. In this respect, the usefulness of the fuel statistical representation is to allow the investigation of MC-fuel drop/flow interaction at higher initial gas temperatures than possible with SC-fuel drops. Comparing the SGPDF and DGPDF models, the latter permits simulation of situations where the drop evaporation is larger than in the former, thus allowing for the possibility of the gas phase to contain substantial vapor that could condense on the drops. It is this physics of the MC fuels at larger gas temperatures than investigated in the previous SC-fuel low Reynolds number study of Miller and Bellan[14] and in the transitional study of Okong'o and Bellan[15] that is here of interest.

This investigation is conducted using the Direct Numerical Simulation (DNS) methodology wherein all scales of the flow are resolved. This methodology was initially devised for single phase flows and was extended by Boivin et al.[16] to two-phase flows with particles that are much smaller than the Kolmogorov scale and which have a volumetrically small loading ($\simeq 10^{-3}$). Indeed, Boivin et al.[16] showed that the drops can be treated as point sources of mass, momentum and energy from the gas-phase perspective, and thus it is then appropriate to perform simulations using a gas-phase resolution that is adequate for single-phase flow, by following the gas phase in an Eulerian frame and tracking the drops in a Lagrangian frame. The terminology DNS, while not strictly accurate, is traditionally applied to such simulations, and several recent studies have used this DNS methodology.[16–20] The present focus is on the influence of the fuel type, of the freestream gas temperature and composition, and of the initial mass loading in determining the flow composition.

Conservation equations

The equations follow in concept the SC study of Miller and Bellan[14] and emulate the SC investigation of Okong'o and Bellan,[15] in that the gas phase is described in an Eulerian frame and the drops are followed in a Lagrangian frame. The drops are assumed much smaller than the Kolmogorov scale, meaning that they can be treated as sources of mass, species, momentum and energy for the gas.[16,20] The MC-fuel composition is described by

$$P(m;\alpha_1,\beta_1,\alpha_2,\beta_2,\epsilon) = (1-\epsilon)f_\Gamma^{(1)} + \epsilon f_\Gamma^{(2)}, \qquad (1)$$

where $f_\Gamma^{(k)} = f_\Gamma(m;\alpha_k,\beta_k)$ with $k = 1, 2$, ϵ is a weighting parameter ($0 \leqslant \epsilon \leqslant 1$), $\int_\gamma^\infty P(m)dm = 1$ and

$$f_\Gamma(m) = \frac{(m-\gamma)^{\alpha-1}}{\beta^\alpha \Gamma(\alpha)} \exp\left[-\left(\frac{m-\gamma}{\beta}\right)\right] \qquad (2)$$

where $\Gamma(\alpha)$ is the Gamma function. The origin of f is specified by γ, and its shape is determined by α and β. Thus, $P(m;\alpha_1,\beta_1,\alpha_2,\beta_2,\epsilon)$ is determined at each time t by the vector $\eta \equiv (\alpha_1,\beta_1,\alpha_2,\beta_2,\epsilon)$; $\gamma_1 = \gamma_2 = \gamma$ is assumed. Harstad et al.[7] have shown that P can be determined by an inverse mapping from its first four moments, θ, ψ, ξ_3 and ξ_4, with a fifth parameter empirically calculated. Thus, at each t, P_l describes the liquid-fuel composition (subscript l denotes the liquid), being drop specific; P_v describes the vapor composition (subscript v denotes the vapor), varying with location. Comparisons between the DGPDF and (32 species) DSA results showed generally very good and at most conditions excellent, agreement.[7]

Gas phase equations

The equation of state

$$p = (\rho R_u T)/m = cR_u T \qquad (3)$$

is combined with Eulerian conservation equations for continuity, momentum, energy, species and first four moments $(\theta_v, \psi_v, \xi_{3v}, \xi_{4v})$ of the composition DGPDF, succinctly written as

$$\partial\Phi/\partial t + \partial\left[\Phi u_j\right]/\partial x_j = S + \partial\left[\Psi(\Phi)\right]/\partial x_j \qquad (4)$$

where

$$\Phi = \{c, cmu_i, cme_t, cX_v, cX_v\theta_v, cX_v\psi_v, cX_v\xi_{3v}, cX_v\xi_{4v}\} \qquad (5)$$

$$S = \{S_{\text{mole}}, S_{\text{mom},j}, S_{\text{en}}, S_{\text{mole}}, S_{\text{mass}}, S_\psi, S_{\xi_3}, S_{\xi_4}\} \qquad (6)$$

$$\Psi(\Phi) = \{cm\mathcal{D}\frac{\partial}{\partial x_j}\left[\frac{X_v}{m}\left(1-\frac{\theta_v}{m_a}\right)\right],$$
$$p\delta_{ij} - \tau_{ij},$$
$$-u_i\tau_{ij} - \lambda\frac{\partial T}{\partial x_j} + \sum_{\zeta=1}^{N} J_{D\zeta,j}\left(h_\zeta - h_a\right),$$
$$cm\mathcal{D}\frac{\partial}{\partial x_j}\left(\frac{X_v}{m}\right), cm\mathcal{D}\frac{\partial}{\partial x_j}\left(\frac{X_v\theta_v}{m}\right),$$
$$cm\mathcal{D}\frac{\partial}{\partial x_j}\left(\frac{X_v\psi_v}{m}\right), cm\mathcal{D}\frac{\partial}{\partial x_j}\left(\frac{X_v\xi_{3v}}{m}\right),$$
$$cm\mathcal{D}\frac{\partial}{\partial x_j}\left(\frac{X_v\xi_{4v}}{m}\right)\} \quad (7)$$

where c is the molar density, x_i is the i^{th} coordinate, $\mathbf{u}$ is the velocity, X is the mole fraction, $m = \theta_v X_v + m_a(1-X_v)$ is the molar mass where m_a is the carrier gas molar weight (subscript a denotes the carrier gas), $\mathcal{D}$ is an effective diffusion coefficient, p is the pressure, τ_{ij} is the viscous stress tensor, δ_{ij} is the Kronecker symbol, $e_t = e_k + e_{int} = u_iu_i/2 + h - p/\rho$ is the total energy of the gas, $\rho = mc$ is the mass density, h is the enthalpy, λ is the thermal conductivity, T is the gas temperature and R_u is the universal gas constant. The last term in flux of the energy equation is the portion of the heat flux due to molar fluxes. The source terms, $S_{\text{mole}}, S_{\text{mom},j}, S_{\text{en}}, S_{\text{mass}}, S_\psi, S_{\xi_3}$ and S_{ξ_4} arise from the coupled interaction of drops and gas, and are given below.

Drop equations

All drops are individually simulated. Under the assumptions of quasi-steady gas phase with respect to the liquid phase, justified by $\rho/\rho_l = O(10^{-3})$,[22] and of uniform internal drop properties, justified by the relatively small evaporation rate[21] (criterion checked *a posteriori*), the Lagrangian conservation equations for each drop position χ, velocity $\mathbf{v}$, energy, mass $M_d = \pi\rho_l D^3/6$ (subscript d denotes the drop) where D is the drop diameter, and composition are

$$\frac{d\chi_i}{dt} = v_i, \quad \frac{dv_i}{dt} = \frac{F_i}{M_d} \quad (8)$$

$$M_dC_{pl}\frac{dT_d}{dt} = \underbrace{\frac{\lambda Nu}{D}\frac{\ln(1+B_T)}{B_T}A\left(T-T_d\right)}_{Q_{\text{conv-diff}}} + \underbrace{\dot{m}_d\frac{L_{veff}}{B}}_{Q_{\text{evap}}} \quad (9)$$

$$\dot{m}_d \equiv \frac{dM_d}{dt} = -\frac{Sh}{3\text{Sc}}\frac{M_d}{\tau_d}\frac{\ln(1+B)}{B} \quad (10)$$

$$\frac{d\xi_{nl}}{dt} = \frac{3\theta_l}{2BD^2}\frac{dD^2}{dt}\{[\frac{X_v}{m} - \frac{X_v^{(s)}}{m^{(s)}}(1+B)]\xi_{nl} + \frac{X_v^{(s)}\xi_{nv}^{(s)}}{m^{(s)}}(1+B) - \frac{X_v\xi_{nv}}{m}\} \quad (11)$$

for $n = 1,2,3,4$, where the gas phase at the drop location, interpolated from the Eulerian solution, acts as the drop far field. $F_i = (M_d/\tau_d)\,f_1\,(u_i - v_i)$ where $\tau_d = \rho_l D^2/(18\mu)$ is the particle time constant for Stokes flow, T_d is the drop temperature, $A = \pi D^2$ is the drop-surface area and μ is the viscosity of the carrier gas; $\text{Pr} = \mu C_p/(\lambda m)$, where C_p is the heat capacity at constant pressure, and $Sc = \mu/(\rho\mathcal{D})$ are the Prandtl and the Schmidt numbers respectively. The Nusselt, Nu, and the Sherwood, Sh, numbers are semi-empirically modified using the Ranz-Marshall correlations, accounting for convective heat and mass transfer effects,[14] with the similarity assumption $Nu = 2 + 0.552\ \text{Re}_{sl}^{1/2}\,(\text{Pr})^{1/3}, Sh = 2 + 0.552\ \text{Re}_{sl}^{1/2}\,(Sc)^{1/3}$. f_1, given in,[14] is an empirical correction to Stokes drag accounting for both finite droplet Reynolds numbers (slip Reynolds number $\text{Re}_{sl} = |\mathbf{u}-\mathbf{v}|\,\rho D/\mu$ where $(\mathbf{u}-\mathbf{v})$ is the slip velocity) and a Reynolds number based on the evaporation-due blowing velocity. $B = (Y_v^{(s)} - Y_v)/(1 - Y_v^{(s)})$ is the Spalding number, where $Y_v = X_v\theta_v/m$ is the vapor mass fraction and $(1+B_T) = (1+B)^{1/Le}$ with Le being the Lewis number, L_{veff} is the effective latent heat[7] and the superscript (s) denotes the drop surface. At this surface, the classical drop boundary conditions of temperature equality, and mass, species, momentum and energy flux conservation[22] apply and Raoult's law relates (ideal-mixture assumed) the drop and gas PDFs

$$P_v^{(s)} = \frac{p_{atm}}{X_v^{(s)}p}\exp\left[\frac{mL_v(m)}{R_uT_b(m)}\left(1-\frac{T_b(m)}{T_d}\right)\right]P_l^{(s)}. \quad (12)$$

where $L_v(m)$ and $T_b(m)$ are the latent heat and the normal boiling point correlated as functions of m,[7] and $p_{atm} = 1atm$.

Source terms

The source-term-vector components of eq. 6 are

$$S_r = -\sum_{q=1}^{N}\frac{w_q}{\Delta V_q}[\Lambda_r]_q \quad (13)$$

$$\Lambda = \{\frac{d\mathcal{N}}{dt}, F_j + \frac{d(\mathcal{N}\theta_l)}{dt}v_j, v_jF_j + Q_{\text{conv-diff}} + Q_{\text{evap}} + \dot{m}_d\left(\frac{v_jv_j}{2} + C_{pl}T_d\right), \frac{d}{dt}(\mathcal{N}\theta_l), \frac{d(\mathcal{N}\psi_l)}{dt}, \frac{d(\mathcal{N}\xi_{3l})}{dt}, \frac{d(\mathcal{N}\xi_{4l})}{dt}\} \quad (14)$$

where $\mathcal{N} = M_d/\theta_l$ is the number of moles in the drop, N is the number of drops, and the summation is over all drops residing within a local numerical discretization volume, ΔV_q. Following SC methodology,[14] a

geometric weighting factor w_q distributes the individual drop contributions to the nearest eight grid points in proportion to their distance from the drop location; because convective effects dominate the species flux term, for MC flows, differential species diffusivity is negligible in transport from the drop location to the grid nodes.

Results

Configuration, boundary conditions and numerics

Displayed in Fig. 1a is the mixing layer configuration showing the streamwise, x_1, cross-stream, x_2, and spanwise, x_3, coordinates with lengths $L_1 = 4\lambda_1 = 29.16\delta_{\omega,0}$, $L_2 = 1.1L_1$, and $L_3 = 4\lambda_3 = 0.6L_1$, with $L_1 = 0.2m$, where λ_1 and λ_3 are forcing wavelengths in the x_1 and x_3 directions, and are used to excite the layer in order to induce roll-up and pairing.[14,23,24] $\delta_{\omega,0} = \Delta U_0 / \langle \partial u_1 / \partial x_2 \rangle$ is the initial vorticity thickness (subscript 0 denotes the initial condition) where $\Delta U_0 = 2U_0$ is the velocity difference across the layer, the brackets $\langle\rangle$ indicate averaging over homogeneous (x_1, x_3) planes, and the initial condition for u_1 is detailed in;[14] the initial mean streamwise velocity has an error-function profile.[14] The drops are randomly distributed throughout $x_2 < 0$ with uniform number density and uniform temperature $T_{d0} < T_0$, where T_0 is the initial uniform gas temperature; thus drop heating and evaporation ensues. The mean drop number density profile is smoothed near the center-line, $x_2 = 0$, using an error function profile. Table 1 summarizes the initial conditions. The initial drop slip velocity with respect to the gas is null, and the initial drop-size distribution is polydisperse and specified by the Stokes number, $St = \tau_d \Delta U_0 / \delta_{\omega,0}$. Comparing MC and SC fuel parameters, it is obvious that one cannot have the same ρ_l, D_0 and St_0. Because of the larger ρ_l at same initial St, the MC calculations are initialized with a larger number of drops, N_0, and a smaller D_0 than their SC counterpart. Since St measures the drop/flow interaction, having the same St_0 in all computations means that if differences in the flow evolution occur, they are entirely the result of the SC versus MC aspect. The MC fuels considered are diesel[7] and three kerosenes (Jet A, RP-1 and JP-7) whose composition,[27] provided as a mole fraction versus of the carbon number by Edwards[28] was fitted in PDF form by Harstad and Bellan.[13] All P_{l0} are here SGPDFs, shown in Fig. 1b (mean and variance in Table 1), this being an excellent representation for JP-7 (for which $\varepsilon = 0$), a very good assumption for RP-1 (for which $\varepsilon = 7.35 \times 10^{-3}$) and an approximation for Jet A (for which $\varepsilon = 0.1357$);[13] this choice means that if P_{l0} evolves into a DGPDF, this would entirely be the result of condensation on the drops. The PDF of the SC fuel (not shown) used for comparison, n-decane, would simply be a delta function at $m = 142$kg/kmol, however, since a delta function is computationally untractable, the SC model of Okong'o and Bellan[15] is used instead. N-decane simulations at $T_0 = 400$K led to a substantial number of drops being evaporated before the second pairing, owing to the single value of $T_b = 447.7$K close to T_0, and thus the results were not conducive to investigating drop-flow interactions; this case was thus not included in the study. All thermodynamic properties were calculated as in Harstad et al.[7,24] The mass loading, ML, is the total mass of the liquid relative to the total mass of the gas in the laden stream.

Initially, the gas phase consists of a carrier gas with a trace of vapor, X_{v0}. The free-stream velocity $U_0 = M_{c,0} a_{C,0}$ is calculated from a specified value of the convective Mach number $M_{c,0}$ based on the carrier gas initial speed of sound $a_{C,0} = \sqrt{R_C T_0 C_{p,C}/C_{v,C}}$ at the initial uniform pressure. The specified value of the initial Reynolds number, $\mathrm{Re}_0 = \rho_0 \Delta U_0 \delta_{\omega,0}/\mu$, where ρ_0 is the initial gas density, is used to calculate μ. The thermal conductivity and diffusivity are then computed using this value of μ and (constant) specified values of $\mathrm{Pr} = Sc$, computed as in Miller et al.[30] For each MC fuel, the freestream initial vapor composition is found from a single-drop simulation in air at the specified T_0 by choosing it to be the first-time-step surface-vapor composition; this choice means that all simulations are initiated with the a uniform vapor composition adjacent to the drops.

The boundary conditions in the x_1 and x_3 directions are periodic, and adiabatic slip-wall conditions in the x_2 direction previously derived[25,26] were here adapted to the DGPDF CT model for MC mixtures. Drops reaching the slip walls are assumed to stick to them.

The equations were solved using an eight-order central finite difference discretization in space and a fourth-order Runge-Kutta for temporal advancement. The grid resolution is listed in Table 1. A fourth-order Lagrange interpolation procedure was used to obtain gas-phase variable values at drop locations. Drops whose mass decreased below 3% of M_d were removed from the calculation. The perturbations used to excite the layer are described elsewhere;[14,23] their relative amplitudes with respect to the circulations are 10% and 2.25% in the spanwise and streamwise directions, respectively. The evolution of the layer comprises two pairings for the four initial spanwise vortices to form a single vortex.

Global layer evolution

The layer growth, measured by the momentum thickness, δ_m, calculated as

$$\delta_m = \frac{\int_{x_2,\min}^{x_2,\max} \left[\langle \rho u_1 \rangle_{x_2,\max} - \langle \rho u_1 \rangle\right] \left[\langle \rho u_1 \rangle - \langle \rho u_1 \rangle_{x_2,\min}\right] dx_2}{\left(\langle \rho u_1 \rangle_{x_2,\max} - \langle \rho u_1 \rangle_{x_2,\min}\right)^2} \tag{15}$$

Case	fuel	T_0	ρ_{l0}	$\{\{D_0\}\} \times 10^{-4}$	θ_{l0} / σ_{l0}	θ_{v0} / σ_{v0}	X_{v0}	$N_0 \times 10^3$
SCdec375	n−decane	375	642	1.365	142 / NA	142 / NA	10^{-4}	580
MCdie375	diesel	375	828	1.202	185.0 / 43.0	140.0 / 28.0	10^{-4}	670
MCdie375x	diesel	375	828	1.202	185.0 / 43.0	140.0 / 28.0	10^{-3}	670
MCdie400	diesel	400	828	1.164	185.0 / 43.0	140.0 / 28.0	10^{-4}	690
MCdie425	diesel	425	828	1.129	185.0 / 43.0	140.0 / 28.0	10^{-4}	720
MCjetA375	Jet A	375	800	1.223	161.0 / 29.7	131.4 / 22.4	10^{-4}	675
MCjetA400	Jet A	400	800	1.184	161.0 / 29.7	131.4 / 22.4	10^{-4}	695
MCrp1375	RP-1	375	800	1.223	165.2 / 17.7	153.5 / 14.8	10^{-4}	675
MCrp1400	RP-1	400	800	1.184	165.2 / 17.7	153.5 / 14.8	10^{-4}	695
MCjp7375	JP-7	375	800	1.223	167.1 / 19.2	153.7 / 15.7	10^{-4}	675
MCjp7400	JP-7	400	800	1.184	167.1 / 19.2	153.7 / 15.7	10^{-4}	695

Table 1 Initial conditions. T_0 in degrees K, ρ_{l0} in kg/m^3, D_0 in m and mean molar weights and standard deviations in kg/kmol. In all simulations, $M_{c,0}$=0.4, $\delta_{\omega,0}$=6.859×10^{-3}m, $\{\{St_0\}\}$=3 and $\{\{(St_0 - \{\{St_0\}\})^2\}\}^{1/2}$=0.5, Re$_0$ = 200, ML_0 = 0.2, $X_{v0} = 10^{-4}$, T_{d0}=345K, γ=86kg/kmol for diesel, γ=41kg/kmol for Jet A, and γ=93kg/kmol for RP1 and JP7, the grid=200×224×120, and CPU time $\simeq$ 792 hours on a SGI Origin 2000 and 274 hours on a cluster with Intel Itenium2 processors.

where $x_{2,\max} = L_2/2$ and $x_{2,\min} = -L_2/2$ are the slip wall coordinates, peaks at $t^* \equiv t\Delta U_0/\delta_{\omega,0} = 95$ independently of the drop composition, as shown in Fig. 2a depicting $\delta_m/\delta_{\omega,0}$ for all runs having $T_0 =$ 375K (results for $T_0 = 400$K are similar). Figure 2b illustrates $\delta_m/\delta_{\omega,0}$ for n-decane and all diesel runs, and in conjuction with Fig.1a leads to the conclusion that there is little $\delta_m/\delta_{\omega,0}$ sensitivity to changes in X_{v0} by an order of magnitude or variation in T_0 of up to 13%, although with increasing T_0 the layer becomes slightly more difficult to entrain after the first pairing. The product thickness, δ_P

$$\delta_P = \int_0^{L_3} \int_{x_2,\min}^{x_{2,\max}} \int_0^{L_1} \rho \left[2 \min\left(Y_V, Y_C\right)\right] dx_1 dx_2 dx_3, \tag{16}$$

measuring the global mixing, is plotted in Figs. 2c and 2d. In contrast to $\delta_m/\delta_{\omega,0}$, δ_P demonstrates substantial variability with the initial conditions and the specific fuel. For $T_0 = 375$K, Fig. 2c, n-decane displays the best global mixing, this being due to its higher evaporation rate (see below) generally followed by Jet A, RP1, JP7 and diesel. Differences between the simulations with different fuels occur early in the layer evolution, and this high δ_P sensitivity may therefore constitute a good experimental diagnostic for comparing fuels. The early higher δ_P for Jet A compared to n-decane results from the initially higher evaporation rate of the former, as species more volatile than n-decane egress the drops. The final ordering of δ_P values is entirely correlated with the fuel saturation curve; this saturation curve is fixed for n-decane but is continuously evolving with time for MC fuels due to the change in composition. Among the diesel runs, δ_P increases with increasing X_{v0} because despite the reduced drop evaporation rate (see below) the larger Y_{V0} contributes to the larger vapor mass in the domain (not shown). When comparing all diesel and n-decane simulations, in Fig. 2d, δ_P increases with T_0, as can be seen for diesel for $T_0 = 375$K, 400K and 425K, which results from the larger evaporation rate at higher T_0. It is also apparent that δ_P for diesel at the highest $T_0 = 425$K is still inferior to the value for n-decane at 375K, this being due to the diesel much smaller volatilty. This indicates that SC fuels are poor simulants of MC fuels for the purpose of phenomena associated with phase change.

Rotational characteristics of the layer are depicted in Fig. 3, the positive spanwise vorticity, $\langle\langle\omega_3^+\rangle\rangle$ (Figs. 3a, 3c, 3e), and the enstrophy, $\langle\langle\omega_i\omega_i\rangle\rangle$ (Figs. 3b, 3d, 3f), where $\langle\langle\rangle\rangle$ denotes averaging over all grid points. Initially null, ω_3^+ is a measure of the small-scale activity; $\omega_i\omega_i$ is related to stretching and tilting which is an important mechanism for turbulence production. For all simulations, $\langle\langle\omega_3^+\rangle\rangle\, \delta_{\omega,0}/\Delta U_0$ grows to an initial peak, at around the time of the first pairing, decreases and then grows again to a higher second peak, after which it declines. The time of the second peak approximately corresponds to the time of the second pairing. N-decane has a slightly higher growth than diesel between roll-up and the middle of the second paring, and past this pairing exhibits a decline, unlike the MC fuels (Fig. 3a). Diesel has slightly inferior peak than all other fuels, whose value seems insensitive to X_{v0} in the studied range (Fig. 3a). Since the diesel has a similar ρ_l as the other MC fuels and the simulations are initiated with similar N_0 and $\{\{D_0\}\}$ ($\{\{\ \}\}$ denotes ensemble averaging over the drops), it appears that there may be composition effects at play, which persist at the larger $T_0 = 400$K (Fig. 3c). With increasing T_0, $\langle\langle\omega_3^+\rangle\rangle$ increases at the second peak (Fig. 3e), and at the higher T_0 values, the second peak assumes a longer lifetime and leads to higher growth thereafter. As for $\langle\langle\omega_i\omega_i\rangle\rangle\,(\delta_{\omega,0}/\Delta U_0)^2$, its peak is smaller for n-decane than for all MC-fuels (Fig. 3b) with a stronger differentiation between diesel and kerosenes than for $\langle\langle\omega_3^+\rangle\rangle$, a result that is invariant with T_0 (Fig. 3d) and which confirms the fuel-specific enstrophy evolu-

tion (Figs. 3d and 3 f).

To explore the reasons for the amplification in vortical activity with increased T_0, the budgets of the conservation equations for ω and $\omega \cdot \omega$

$$\frac{D\omega}{Dt} = (\omega.\nabla)\mathbf{u} - (\nabla \cdot \mathbf{u})\omega - \nabla(\frac{1}{\rho}) \times \nabla p + \nabla \times (\frac{1}{\rho}\nabla \cdot \bar{\bar{\tau}}) + \nabla \times (\frac{1}{\rho}\mathbf{S}_{\text{mom}}) - \nabla \times (\frac{1}{\rho}S_{\text{mass}}\mathbf{u}) \quad (17)$$

$$\frac{D(\omega \cdot \omega)}{Dt} = 2\omega \cdot (\omega \cdot \nabla\mathbf{u}) - 2(\nabla \cdot \mathbf{u})\omega \cdot \omega - 2\omega \cdot [\nabla(\frac{1}{\rho}) \times \nabla p] + 2\omega \cdot [\nabla \times (\frac{1}{\rho}\nabla \cdot \bar{\bar{\tau}})] + 2\omega \cdot [\nabla \times (\frac{1}{\rho}\mathbf{S}_{\text{mom}})] - 2\omega \cdot [\nabla \times (\frac{1}{\rho}S_{\text{mass}}\mathbf{u})] \quad (18)$$

were assessed, where D/Dt is the substantial derivative. Depicted in Fig. 4 are the (x_1, x_3) homogeneous plane-average budget RMS of the streamwise and spanwise vorticity and of the vorticity magnitude for the diesel simulations at $T_0 = 375$K and 420K at $t^* = 95$. Irrespective of the considered vorticity, the maximum contribution is that of the stretching and tilting term, followed by the stresses and then by $\mathbf{S}_{\text{mom}}$, with all other terms being negligible. The difference between the $T_0 = 375$K and 400K simulations is that for the latter the stretching and tilting term has larger peaks for ω_1 and $\omega \cdot \omega$ in the middle of he layer and that the $\mathbf{S}_{\text{mom}}$ contribution is smaller. For ω_1, $\mathbf{S}_{\text{mom}}$ contributes through the entire layer, with similar magnitude peaks in the lower stream and in the moddle of the layer, and a larger peak in upper stream ; for $\omega \cdot \omega$, the stretching and tilting term and the stresses almost equally dominate the contribution in most of the layer with the exception of a specific location in the upper stream where $\mathbf{S}_{\text{mom}}$ has the largest magnitude. To examine the phenomenon responsible for the magnitude of $\mathbf{S}_{\text{mom}}$, this term was decomposed as

$$\mathbf{S}_{\text{mom}} = -\sum_{q=1}^{N} \frac{w_q}{\Delta V_q}\left[\mathbf{F} + \left(\theta_l \frac{d\mathcal{N}}{dt} + \mathcal{N}\frac{d\theta_l}{dt}\right)\mathbf{v}\right]_q = \mathbf{S}_{\text{mom,drag}} + \mathbf{S}_{\text{mom,evap}} + \mathbf{S}_{\text{mom,mean}} \quad (19)$$

and budgets of the eq. 19 (not illustrated) show the dominating term to be $\mathbf{S}_{\text{mom,drag}}$, indicating that the source terms contributions in the budgets of eqs. 17 and 18 are mostly of dynamic nature for these conditions. That is, with increasing T_0, the drops are smaller at $t^* = 95$ due to the earlier evaporatioon and the smaller drag counteracts to a reduced extent the formation of small scales, which results in an augmented vortical activity of the flow. Although for the conditions of the present simulations $\mathbf{S}_{\text{mom,evap}}$ and $\mathbf{S}_{\text{mom,mean}}$ are small compared to $\mathbf{S}_{\text{mom,drag}}$, one can conceive of situations where the rate of change in drop composition is substantial, and it could affect the vorticity evolution of the flow. The possibility of substantial thermodynamic contributions from these sources to the vorticity shows the tight dynamics/thermodynamics coupling in these compressible flows.

To develop an understanding of the state of the flow at $t^* = 95$, flow visualizations are examined next.

Flow visualizations

Illustrated in Fig. 5 is the drop number density calculated as an Eulerian field from the Lagrangian distribution

$$\rho_n = \sum_{q=1}^{N_d} \frac{w_q}{\Delta V_q}. \quad (20)$$

The plots depict the between-the-braid plane $x_3/\delta_{\omega,0} = 8.75$ distribution for several simulations at $t^* = 95$. In all cases, a complex drop organization is observed, with void regions corresponding to locations of high vorticity (not shown); these voids are profiled by high ρ_n regions that correspond to high strain locations.[31] The structural complexity of the drop organization is insensitive to T_0 (Figs. 5a, 5c and 5e), which is the result of two counteracting effects: first, the larger N_0 at same St_0 means that more drops interact with the flow which creates more local non-uniformities through the drag action, however, $\{\{D_0\}\}$ being sligthly smaller combined with the larger T_0 means that the drop lifetime is reduced, which reduces the drops/flow interaction time. The $\mathbf{S}_{\text{mom}}$ peaks observed in Fig. 4 occur in the regions of highest ρ_n. Increasing X_{v0} (Figs. 5a and 5b) decreases the complexity of the drop organization, this resulting from the opposite effects of the longer drop lifetime which increases the interaction with the flow and promotes non-uniformities and the difficulty of the flow to transport a larger mass loading; apparently, the latter effect dominates at $t^* = 95$. Finally, comparisons among diesel, Jet A and RP-1 (JP-7 contours are similar to the other kerosenes) in Figs. 5a, 5d and 5f, show the specific characteristics of the diesel drop distribution when compared to the kerosenes; some of these differences may result from the marginally smaller N_0 and $\{\{D_0\}\}$ for diesel at same St_0, which are difficult to separate from the other influences on the flow.

The Y_v contours are shown in Fig. 6 for selected simulations. In all cases, the lower stream has the highest vapor mass fraction, the smallest mass fraction is in the upper stream and the mixing layer contains a very inhomogeneous mixture. Compared to n-decane, diesel produces a much smaller Y_v, with a maximum value that is less than 60% of that for n-decane (ρ values are similar). With increasing T_0, the layer entrains hotter gas, and the promoted evaporation increases Y_v.

As X_{v0} increases, there is naturally a larger maximum Y_v, but not additively with respect to two X_{v0} values because of intervening transport effects. Finally, Jet A being more volatile than diesel, Y_v is larger, representing the trend for all kerosenes. For SC fuels, the Y_v information completes the state of the vapor, however, for MC fuels the composition is necessary to entirely characterise the vapor. For MC fuels, the mixture composition is displayed in Fig. 7 for θ_v and Fig. 8 for σ_v. Independent of the simulation, both θ_v and σ_v exhibit strong inhomogeneities. For diesel at $T_0 = 375$K with $X_{v0} = 10^{-4}$, the smallest θ_v value is in the upper stream and corresponds to the initial condition. The next larger values are in the lower stream because this is where the drops initially reside and thus where the more volatile species evaporate. The mixing layer contains the intermediate molar weight species which evaporate only after the drops have already been entrained into the layer. The largest θ_v value is within the layer at the location of the highest ρ_n because the heaviest molar weight species are the least volatile and evaporate only after the drop structure has been established. The smallest σ_v is in the lower stream and then within the layer where ρ_n is small or where ρ_n is large but $\{\{D_0\}\}$ is (conjectured) small indicating that most species have evaporated. Intermediate values of σ_v are found in the upper stream where species from the layer may escape, changing the initially uniform composition, and also in the layer adjacent to the location of the largest ρ_n because the heaviest evaporating species transported from the largest ρ_n location will make a relatively large impact on the mean. The largest σ_v is at the location of the largest ρ_n where the heaviset species evolve from the drops. Thus, a composition stratification is established, much as had been observed for laminar flow combustion with two species, where the simulations were performed with computational instead of physical drops.[32] Information not available in such binary-fuel computations is presented by σ_v which exhibits strong local variations, the smaller ones being in the lower stream, and the largest in the regions of highest θ_v.

With increasing X_{v0}, the maximum value of θ_v decreases and that of σ_v increases indicating a reduced evaporation rate which did not allow the evolution of the heavier species observed at the lower X_{v0}, and thus also less variation in the composition. When T_0 is larger, the maximum θ_v increases and the range of σ_v augments because the larger evaporation rate allows increasingly heavier species to evolve from the drops, which increases σ_v. Finally, at same T_0, both θ_v and σ_v are fuel specific. The narrower PDF of Jet A, shifted to the lower m regime with respect to diesel, results in smaller maximum θ_v and a shifted range of σ_v towards lower values; a more non-uniform distribution of σ_v is also apparent. For RP-1, its narrower PDF with respect to both diesel and Jet A leads to a decreasd range for both θ_v and σ_v while for JP-7, its wider PDF with respect to RP-1 but narrower than Jet A leads or both θ_v and σ_v to a range of values intermediary to those of the two other kerosenes. Thus, the composition of the vapor is distinct for each of the fuels and the trends can be directly traced to its original composition. This information is inherently unavailable in SC simulations, and threfore caution must be exercised in using SC fuels as surrogate for MC fuels, either in simulations or in experiments.

Drop evolution

Shown in Fig. 9 are ensemble averages portraying the evolution of the drop characteritics. For n-decane, T_{sat} is constant and thus is not plotted in Fig. 9a. For all MC fuels, $\{\{T_{sat}\}\}/T_{sat,0}$ increases rapidly during rollup as the most volatile species egress the drops and then gradually asymptotes as the drop composition becomes more uniform. The least increase, $\sim 1.5\%$, is observed for RP-1 and JP-7 at $T_0 = 375$K and the larger $T_0 = 400$K only slightly elevates $\{\{T_{sat}\}\}/T_{sat,0}$ to slightly more than 2%. Jet A, being more volatile than the other two kerosenes, experiences a larger change in $\{\{T_{sat}\}\}/T_{sat,0}$ with about 4.5% and 6% eventual increase at $T_0 = 375$K and 400K, respectively. The diesel profile coincides with that of Jet A at $T_0 = 375$K, which is happenstance from the ensemble averaging; at $T_0 = 400$K, a slightly larger $\{\{T_{sat}\}\}/T_{sat,0}$ is obtained for diesel, and the maximum value is about 6.5%. The distinct behavior of the fuels is noticeable. With increasing T_0, there is a correspondingly larger initial rate of increase in $\{\{T_{sat}\}\}/T_{sat,0}$ as the volatile species evaporate faster, and the ultimate value reached is larger, being almost 9% for $T_0 = 425$K. With increasing X_{v0}, evaporation is slower, which sligtly decreases $\{\{T_{sat}\}\}/T_{sat,0}$. Although the % changes in $\{\{T_{sat}\}\}/T_{sat,0}$ are small, for individual drops they can be much larger, which has an impact on the local composition.

Exmination of $\{\{D^2/D_0^2\}\}$ in Fig. 9e shows that among all fuels, at fixed T_0, the n-decane drops evaporate fastest, reaching about 60% of $\{\{D_0^2\}\}$, which corresponds to about 46% of the initial mass, as shown in Fig. 9f depicting $\{\{M_d/M_{d,0}\}\}$. The diesel drops evaporate slowest, reaching about 71% of the initial mass, and the three kerosenes evaporate at approximately the same rate, 52%-55% of the initial mass. With increasing T_0 the drops evaporate faster and for larger X_{v0} the drops evaporate slower, as expected, however, the small differences among values of $\{\{T_{sat}\}\}/T_{sat,0}$ displayed in Fig. 9a translate in much larger differences for $\{\{D^2/D_0^2\}\}$. Moreover, these $\{\{D^2/D_0^2\}\}$ differences are even larger if only the drops in the layer are considered since the lower stream more numerous drops evetually saturate (not shown), which biases the ensemble average value, while the mixing layer drop size continuously decreases.The wide range of resid-

ual mass attained by the drops, from 72% to 38%, is evident.

Presented in Fig. 9c is $\{\{T_d/T_{sat}\}\}$ versus t^*. In all cases, a very mild $\{\{T_d/T_{sat}\}\}$ undulatory behavior is observed, traced to $\{\{T_d\}\}$ (not shown) manifesting evaporative cooling and heating cycles; ensemble averages conditioned on drop location (mixing layer for $x_2/\delta_{\omega,0} \geq -7$; complement is the lower stream) displayed in Fig. 9d show this behavior to be biased by the larger number of drops in $x_2/\delta_{\omega,0} < -7$, as the mixing layer $\{\{T_d\}\}$ continuously increases after the first pairing. The variation of $\{\{T_d/T_{sat}\}\}$ for n-decane (not shown) duplicates the behavior $\{\{T_d\}\}$ as T_{sat} is constant. For the MC fuels, the behavior is due to either the counteracting or concerting effect of T_d and T_{sat}. As the volatiles preferentially leave the drops, $\{\{T_{sat}\}\}$ increases concomitantly with $\{\{\theta_l\}\}/\theta_{l0}$ (shown below). At $T_0 = 375$K, the initial reduction of $\{\{T_d/T_{sat}\}\}$ combines the decrease in T_d with the increase in T_{sat}. At $T_0 > 375$K, two initial behaviors are seen: a reduction in $\{\{T_d/T_{sat}\}\}$ (diesel and Jet A) meaning that the increase in T_{sat} due to the evaporation of lower-m species is larger than the increase in T_d due to drop heating, or an augmentation in $\{\{T_d/T_{sat}\}\}$ (PR1 and JP7) meaning the opposite. The peaks and troughs in $\{\{T_d/T_{sat}\}\}$ emulate those of $\{T_d\}$ indicating that away from the initial condition, the global T_d variation is larger than that of T_{sat}.

The ensemble average Spalding number is presented in Fig. 9b. Jet A being considerably more volatile than the other fuels, the initial $\{\{B\}\}$ for the corresponding simulations is larger; however, for all simulations $\{\{B\}\}$ is small compared to unity and continuously and drastically decreases, verifying *a posteriori* the assumption of internal drop uniform conditions. The largest rate of decline occurs for the diesel simulation with $X_{v0} = 10^{-3}$, consistent with the decreased evaporation. When calculating the ensemble average of B using only the drops in the lower stream, and for all simulations, small negative values reached after the first and second pairings (not shown), indicating that at those times the liquid composition change in the lower stream is dominated by condensation. Except for Jet A, the magnitude of these small values increases with increasing T_0 which is explained by the increasing evaporation rate that brings lighter species into the gas phase which further proceed to condense on the drops. Companion plots of D^2/D_0^2 ensemble averaged over the lower stream (not shown), show an asymptotic value eventually reached, which supports this interpretation.

The evolution of the liquid composition is displayed in Fig. 10 in terms of $\{\{\theta_l\}\}/\theta_{l0}$ and $\{\{\sigma\}\}/\sigma_{l0}$. The initial $\{\{\theta_l\}\}/\theta_{l0}$ surge is accompanied by a drastic reduction in $\{\{\sigma_l\}\}/\sigma_{l0}$ as the volatiles evaporate, and $\{\{\sigma_l\}\}/\sigma_{l0}$ reaches a minimum. This minimum, beyond which $\{\{\sigma_l\}\}/\sigma_{l0}$ continuously increases, coincides with a tapering off in the $\{\{\theta_l\}\}/\theta_{l0}$ increase. Therefore, both evaporation and condensation occur: condensation increases $\{\{\sigma_l\}\}/\sigma_{l0}$ whereas evaporation of the lightest species increases $\{\{\theta_l\}\}/\theta_{l0}$. Most changes in θ_l occur for diesel and Jet A, and are about 10% at $T_0 = 375$K and 13% at $T_0 = 400$K, while the corresponding values for RP-1 and JP-7 are lower than 4% and 6%, respectively (Figs. 10a. and 10c). For the diesel simulation at $T_0 = 425$K, in excess of 17% change in θ_l is observed (Fig. 10e). Minimal sensitivity is exhibited by θ_l to an order of magnitude increase in X_{v0} (Figs. 10a and 10e) because as shown by Harstad et al.,[7] it is the composition of the vapor rather than its mole fraction (in this regime) that impact θ_l; the small decrease in θ_l occurring with increasing X_{v0} results from the reduced evaporation rate which promotes thus a correspondingly smaller change in composition. More sensitivity to all parameters is exhibited by σ_l. At both $T_0 = 375$K and 400K (Figs. 10b and 10d), Jet A has the largest initial decline in $\{\{\sigma_l\}\}/\sigma_{l0}$ (in excess of 7% and 8%, respectively) as the stronger evaporation depletes more of the volatiles compared to the other fuels; with condensation, $\{\{\sigma_l\}\}/\sigma_{l0}$ augments again, and this recovery is stronger with increasing T_0 owing to the larger range of volatile species that may condense. Diesel displays less $\{\{\sigma_l\}\}/\sigma_{l0}$ variation than Jet A during the layer evolution and its initial decline as well as the recovery are smaller. Both RP-1 and JP-7 show the least initial reduction in $\{\{\sigma_l\}\}/\sigma_{l0}$ due to their narrower PDF and the continuous increase past unity indicates that the initial SGPDF peak has been substantially reduced to permit a non-negligible contribution to the PDF by increasingly-lower-m species; the % augmentation of $\{\{\sigma_l\}\}/\sigma_{l0}$ past unity increases with T_0 as the promoted evaporation results in increasingly less volatile species leaving the drops. For diesel, the increasing T_0 leads to a greater effect in the inital $\{\{\sigma_l\}\}/\sigma_{l0}$ reduction and to a larger recovery (Figs. 10f), indicating the strong temperature effect on evaporation and condensation, particularly for the lower-m species, and thus the substantial T_0 infuelnce on the liquid composition.

The conclusion is that fuel specificity is important in determining both the drop characteristics and the liquid composition and that the gas phase temperature has a large impact on the liquid composition. The relatively small variations observed here correspond to the small $(T_0 - T_d)/T_0$ range investigated, and it is predictable that larger variations will occur at higher $(T_0 - T_d)/T_0$.

Vapor composition

Homogeneous-plane averages of θ_v/θ_{v0} and σ_v/σ_{v0} at $t^* = 95$ are displayed in Figs. 11a and 11b and show the fuel-specific variations, although for all fuels the vapor is contained within the mixing layer and the lower stream; the lower stream uniform $\langle\theta_v\rangle/\theta_{v0}$ and

$\langle\sigma_v\rangle/\sigma_{v0}$ is consistent with the saturation discussed above. Diesel evaporation produces the largest change in $\langle\theta_v\rangle/\theta_{v0}$, mainly due to its very wide distribution. The $\langle\theta_v\rangle/\theta_{v0}$ peak coincides with the contour-plot-identified regions of high θ_v; this coincidence is even more pronounced for $\langle\sigma_v\rangle/\sigma_{v0}$ showing first increased heterogeneity with the cross-stream distance, then the reaching of the above-discussed peak, and finally the decay to unity in the upper stream. Similar effects are exhibited by all kerosenes, with the difference that they are much less sensitive to T_0 and that the variations in the cross-stream direction are greatly reduced, both of which are attributed to their narrower initial PDF. At same T_0, the highest $\langle\theta_v\rangle/\theta_{v0}$ is for diesel, and then in decreasing order for Jet A, JP7 and RP1, decreasing with the reduction in their initial PDF width. Of all kerosenes, Jet A produces the largest $\langle\theta_v\rangle/\theta_{v0}$ in the mixing layer, consistent with the wider PDF on the high-m side, but relatively smaller values in the lower stream, consistent with the wider PDF on the low-m side. Similarly, the Jet A $\langle\sigma_v\rangle/\sigma_{v0}$ displays more variation across the layer than the other kerosenes, which is again representative of its wider PDF. Thus, the composition of the gas phase mixture, which is responsible for ignition, combustion and pollutant production is highly variable with the MC fuel and must be captured if accurate predictions from combustion models are desired.

Conclusions

A formulation for describing the composition of MC fuels using a statistical representation has been used to derive a model of many drops evaporating in a flow. This model has been applied to study the evaporation of drops in a three-dimensional temporal mixing layer whose lower stream is initially laden with a collection of randomly distributed polydiperse drops. The layer initially contains four spanwise vortices whose double pairing, promoted by a perturbation, results in the formation of an ultimate vortex. The results have been analyzed to study the layer and drop evolution as well as the state at the highest momentum thickness of the layer. Comparisons are made among simulations performed with a SC fuel (n-decane), diesel and three kerosenes: Jet A, RP1 and JP7. The results show substantial differences between the global and local mixing features of the layers, all of which are traced to the relative initial composition of the fuels. Strong composition nonuniformities in the layer, found for all MC fuels, means that SC fuels cannot capture the necessary species distribution to model combustion. Moreover, the species distribution is fuel-specific, offering the possibility to discriminate between fuel-composition-related combustion efficiency, pollutant formation, corrosion aspects, etc. The simulations show that the identified composition effects are amplified with increasing temperature. Likewise, for Reynolds numbers larger than that of the simulations, evaporation will be enhanced resulting again in amplified composition heterogeneity. Thus, turbulent combustion models must realistically include fuel composition effects.

Acknowledgements

This study was conducted at the Jet Propulsion Laboratory (JPL), California Institute of Technology (Caltech), under the partial sponsorship of the Donors of The Petroleum Research Fund administered by the American Chemical Society through a grant (to JB) for Caltech Post Doctoral Fellow support, the U.S. Department of Energy with Ms. R. Danz and Mr. D. Hooker as contract monitors, under an agreement with the National Aeronautics and Space Administration, and the Air Force Research Laboratory, Wright Patterson Air Force Base with Dr. J. T. Edwards as Technical Monitor. Additional sponsorship was provided by the Office National d'Études et de Recherches Aérospatiales for Post Doctoral support. We wish to thank Dr. K. G. Harstad for helpful discussions. Computational resources were provided by the supercomputing facility at JPL.

References

[1]C. K. Law and H. K. Law, "A d^2-law for multicomponent droplets vaporization and combustion," *AIAA J.* 20 (1982) 522–527.

[2]C. M. Megaridis and W. A. Sirignano, "Numerical modeling of a vaporizing multicomponent droplet," *Proc. Comb. Inst.* 23 (1990) 1413-1421.

[3]K. Harstad and J. Bellan, "A Model of the evaporation of binary-fuel clusters of drops," *Atomization and Sprays* 1 (1991) 367–388.

[4]J. Tamim and W. L. H. Hallett, "A continuous thermodynamics model for multicomponent droplet vaporization," *Chem. Eng. Sci.* 50 (1995) 2933-2942.

[5]W. L. H. Hallett, "A simple model for the vaporization of droplets with large numbers of components," *Combust. Flame* 121 (2000) 334-344.

[6]A. M. Lippert and R. D. Reitz, "Modeling of multicomponent fuels using continuous distributions with application to droplet evaporation and sprays," SAE paper 97FL-468, 1997.

[7]K. G. Harstad, P. C. Le Clercq and J. Bellan, "A statistical model of multicomponent-fuel drop evaporation for many-droplet gas-liquid flow simulations", *AIAA J.*, 41(10) (2003) 1858-1874.

[8]B. Gal-Or, H. T. Cullinan, Jr. and R. Galli, "New thermodynamic-transport theory for systems with continuous component density distributions," *Chem. Eng. Sci.* 30 (1975) 1085-1092.

[9]R. L. Cotterman, R. Bender and J. M. Prausnitz, "Phase equilibria for mixtures containing very many components. Development and application of continuous thermodynamics for chemical process design," *Ind. Eng. Chem. Process Des. Dev.* 24 (1985) 194–203.

[10]C. H. Whitson, "Characterizing hydrocarbon plus fractions," *Soc. Pet. Eng. J.* 23 (1983) 683-694.

[11]M. T. Rätzsch, and H. Kehlen, "Continuous thermodynamics model of complex mixtures," *Fluid Phase Equilibria* 14 (1983) 225-234.

[12]G. F. Chou and J. M. Prausnitz, "Adiabatic flash calculations for continuous or semicontinuous mixtures using an equation of state," *Fluid Phase Equilibria* 30 (1986) 75-82.

[13]K. G. Harstad and J. Bellan, "Modeling evaporation of Jet A, JP-7 and RP-1 drops at 1 to 15 bars", paper F9, Western States Meeting of the Combustion Institute, October 2003, Los Angeles, CA; submitted 2003.

[14]R. S. Miller and J. Bellan, "Direct numerical simulation of a confined three-dimensional gas mixing layer with one evaporating hydrocarbon-droplet laden stream," *J. Fluid Mech.* 384 (1999) 293-338.

[15]N. Okong'o and J. Bellan, Consistent Large Eddy Simulation of a temporal mixing layer laden with evaporating drops. Part I: Direct Numerical Simulation, formulation and *a priori* analysis, *J. Fluid Mech.*, 499 (2004) 1-47.

[16]M. Boivin, S. Simonin and K. D. Squires, "Direct numerical simulation of turbulence modulation by particles in isotropic turbulence," *J. Fluid Mech.* 375 (1988) 235-263.

[17]F. Mashayek and F.A. Jaberi. Particle dispersion in forced isotropic low-Mach-number turbulence. *International Journal of Heat and Mass Transfer*, 42:2823–2836, 1999.

[18]F. Mashayek. Direct numerical simulations of evaporating droplet dispersion in forced low-Mach-number turbulence. *International Journal of Heat and Mass Transfer*, 41(17):2601–2617, 1998.

[19]J. Réveillon and L. Vervisch. Spray vaporization in nonpremixed turbulent combustion modeling: A single drop model. *Combustion and Flame*, 121:75–90, 2000.

[20]F. Mashayek, "Droplet-turbulence interactions in low-Mach-number homogeneous shear two-phase flows," *J. Fluid Mech.* 367 (1998) 163–203.

[21]A. Makino and C. K. Law, "On the controlling parameter in the gasification behavior of multicomponent droplets," *Combust. Flame* 73 (1988) 331-336.

[22]F. A. Williams, *Combustion Theory*, Addison-Wesley, 1965

[23]R. D. Moser and M. M. Rogers, "Mixing transition and the cascade to small scales in a plane mixing layer," *Phys. Fluids A*, **3** (1991) 1128–1134.

[24]R. S. Miller and J. Bellan, "Direct numerical simulation and subgrid analysis of a transitional droplet laden mixing layer," *Phys. Fluids* 12(3) (2000) 650-671.

[25]T. J. Poinsot and S. K. Lele, "Boundary conditions for direct simulations of compressible viscous flows," *J. Comp. Phys.* 101 (1992) 104–129.

[26]M. Baum, T. J. Poinsot and S. K. Lele, "Accurate boundary conditions for multicomponent reactive flows," *J. Comp. Phys.* 116 (1994) 247-261.

[27]T. Edwards, L. Q. Maurice, "Surrogate mixtures to represent complex aviation and rocket fuels," *J. Propul. Power* 17(2) (2001) 461-466.

[28]T. Edwards, private comm. (2002).

[29]K. G. Harstad and J. Bellan, "Modeling evaporation of Jet A, JP-7 and RP-1 drops at 1 to 15 bars", in revision, *Combustion and Flame*, 2003

[30]R. S. Miller, K. Harstad and J. Bellan, "Evaluation of equilibrium and non-equilibrium evaporation models for many-droplet gas-liquid flow simulations," *Int. J. Multiphase Flow* 24 (1998) 1025-1055.

[31]K. D. Squires and J. K. Eaton, "Preferential concentration of particles by turbulence," *Phys. Fluids* A 3 (1991) 1169-1178.

[32]G. Continillo and W. A. Sirignano, "Numerical study of multicomponent fuel spray flame propagation in a spherical closed volume," *Proc. Comb. Inst.* 22 (1988) 1941-1949.

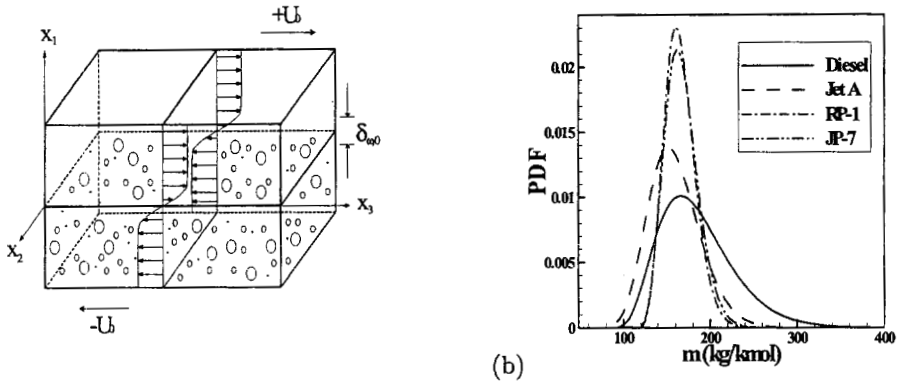

(a) (b)

Fig. 1 Mixing layer configuration (a) and liquid initial PDF for each fuel (b).

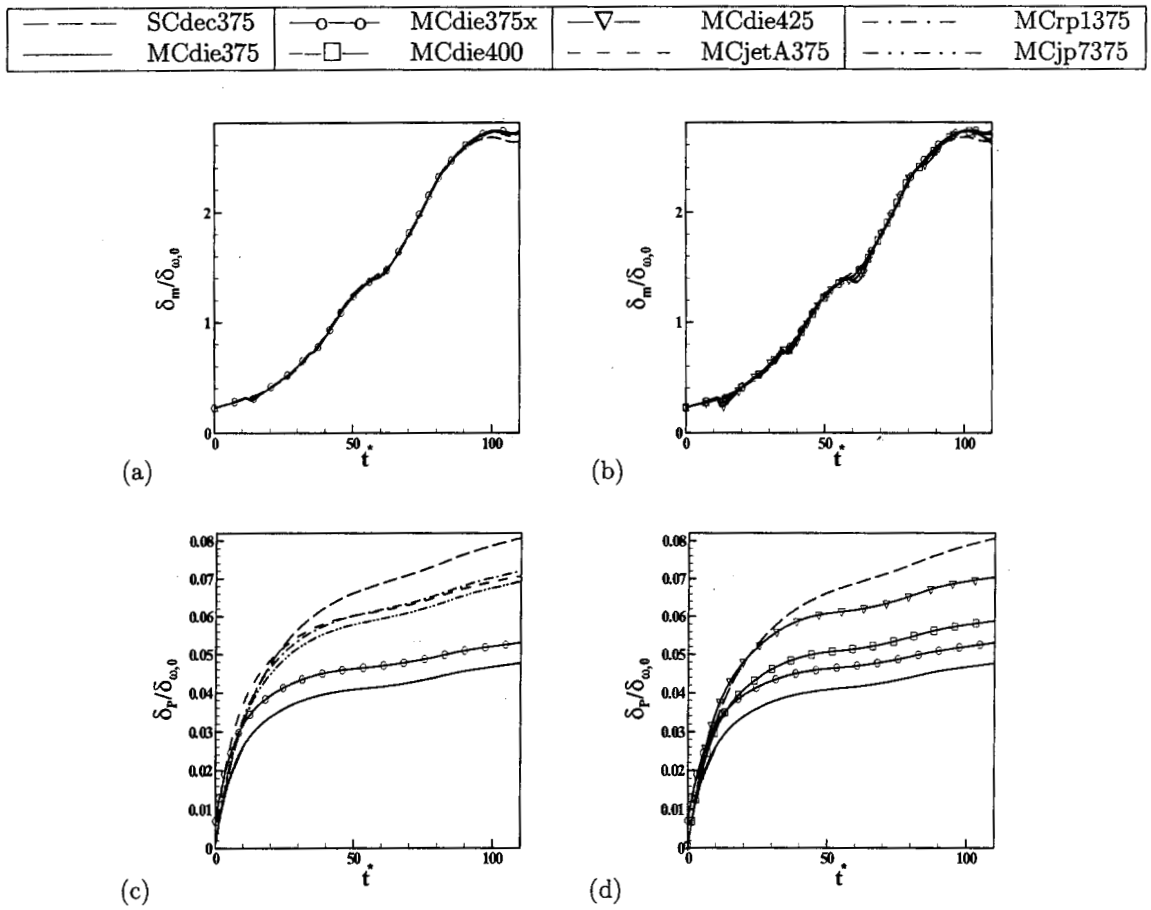

(a) (b) (c) (d)

Fig. 2 Timewise evolution of the momemtum thickness (a,b) and product thickness (c,d) for, a) and c) all simulations having an initial temperature of 375 K, and b) and d) all Diesel-fuel simulations and n-decane.

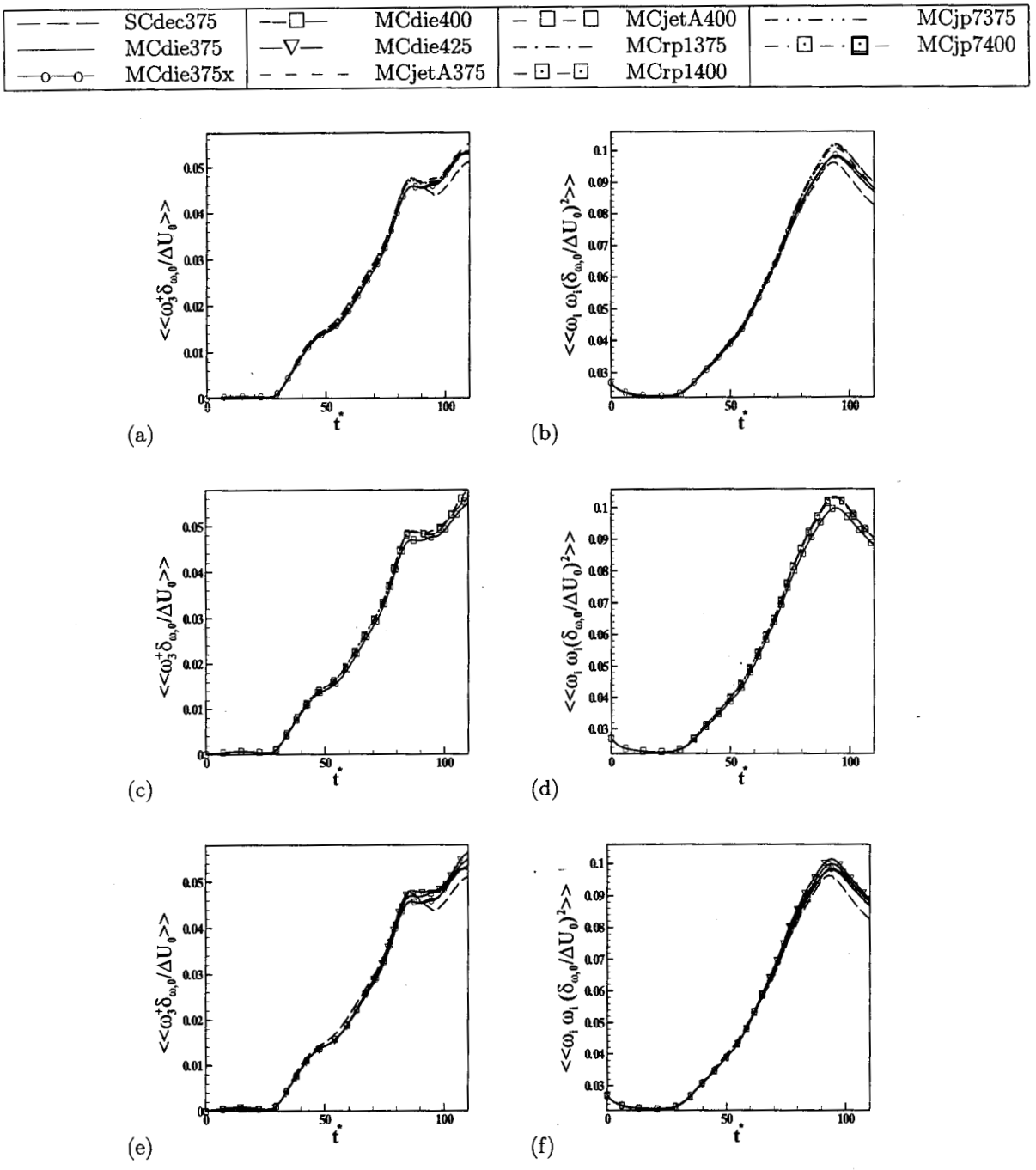

Fig. 3 Timewise evolution of the Eulerian average positive spanwise vorticity (a,c,e) and the enstrophy (b,d,f) for (a) and (b) all simulations having an initial temperature of 375 K, (c) and (d) all simulations having an initial temperature of 400 K, and (e) and (f) all the Diesel-fuel simulations and n-decane.

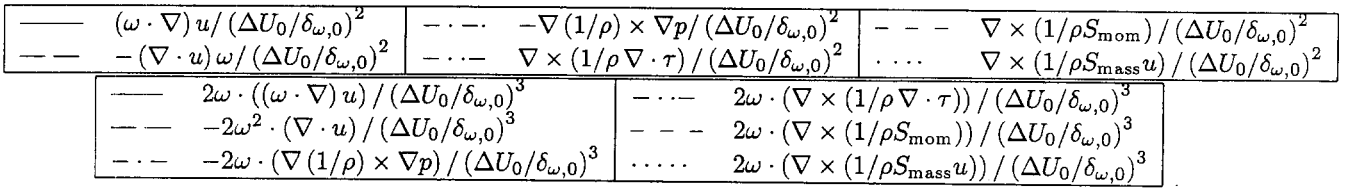

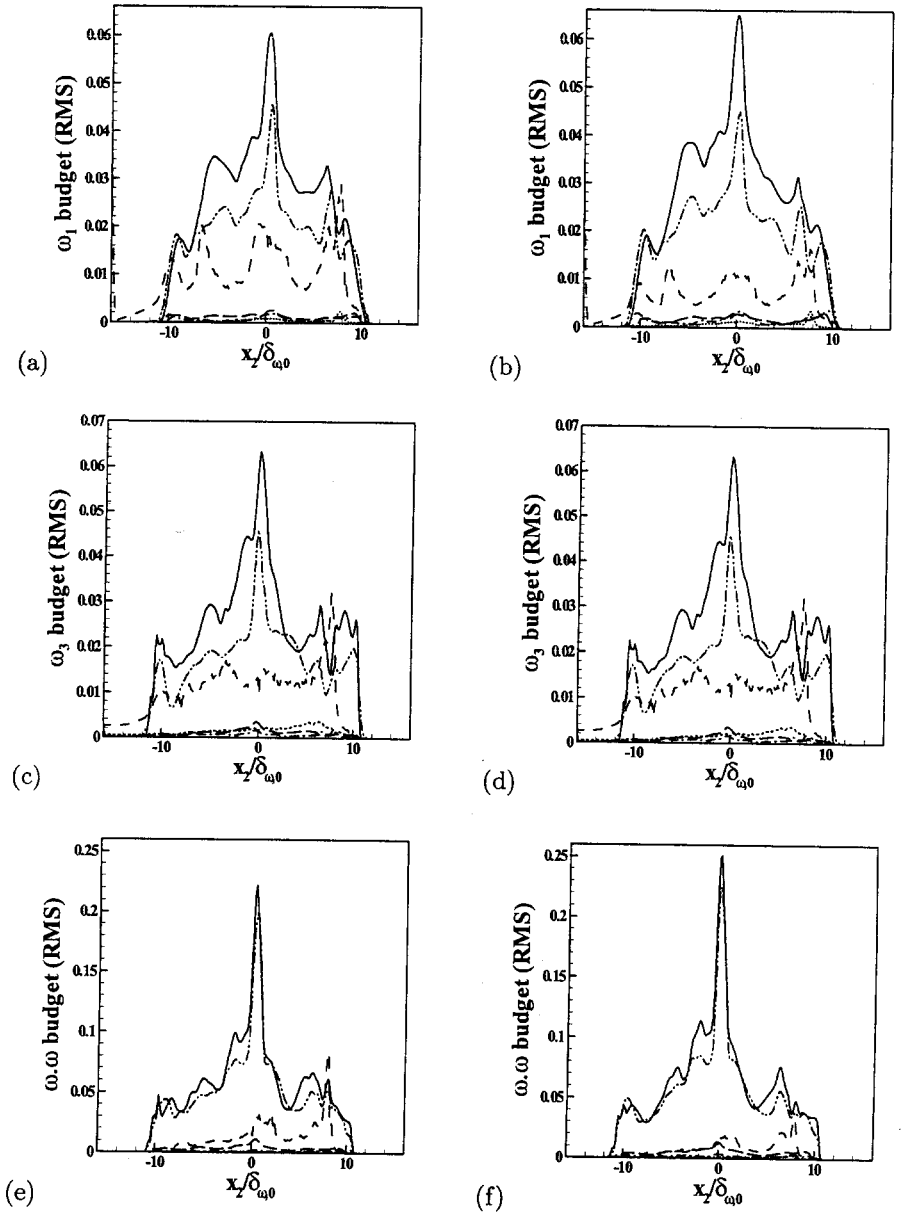

Fig. 4 Streamwise vorticity budget (a,b), cross-stream vorticity budget (c,d), and enstrophy budget (e,f) at $t^* = 95$ for two simulations: (a,c,e) MCdie375 and (b,d,f) MCdie425.The legend for the streamwise and cross-stream vorticity budgets is in the top box. The legend for the enstrophy budget is in the second to the top box.

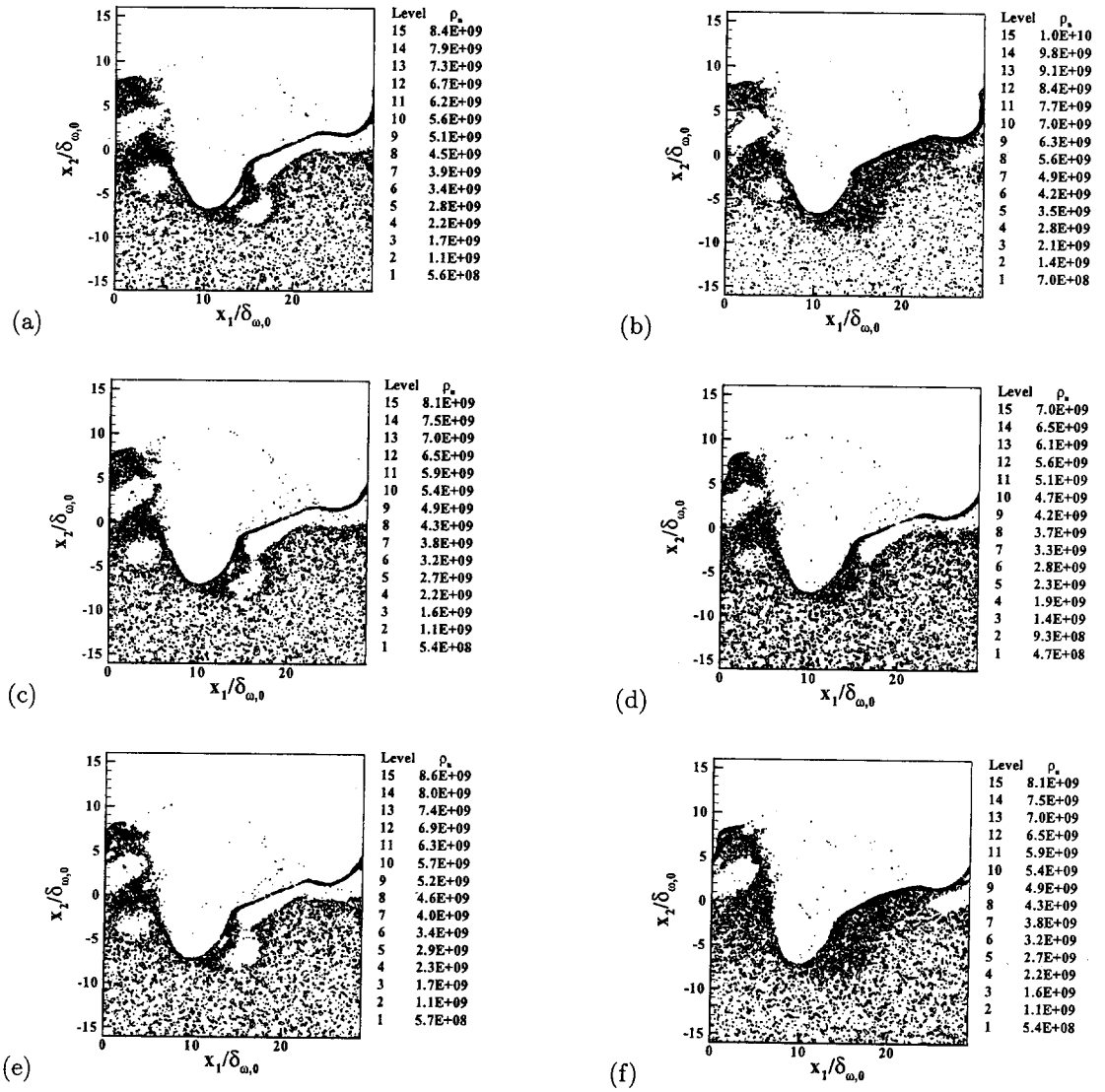

Fig. 5 Contour plots of the drop number density in the between-the-braid plane at $t^* = 95$. MCdie375 (a), MCdie375x (b), MCdie400 (c), MCjetA400 (d), MCdie425 (e), and MCrp1400 (f).

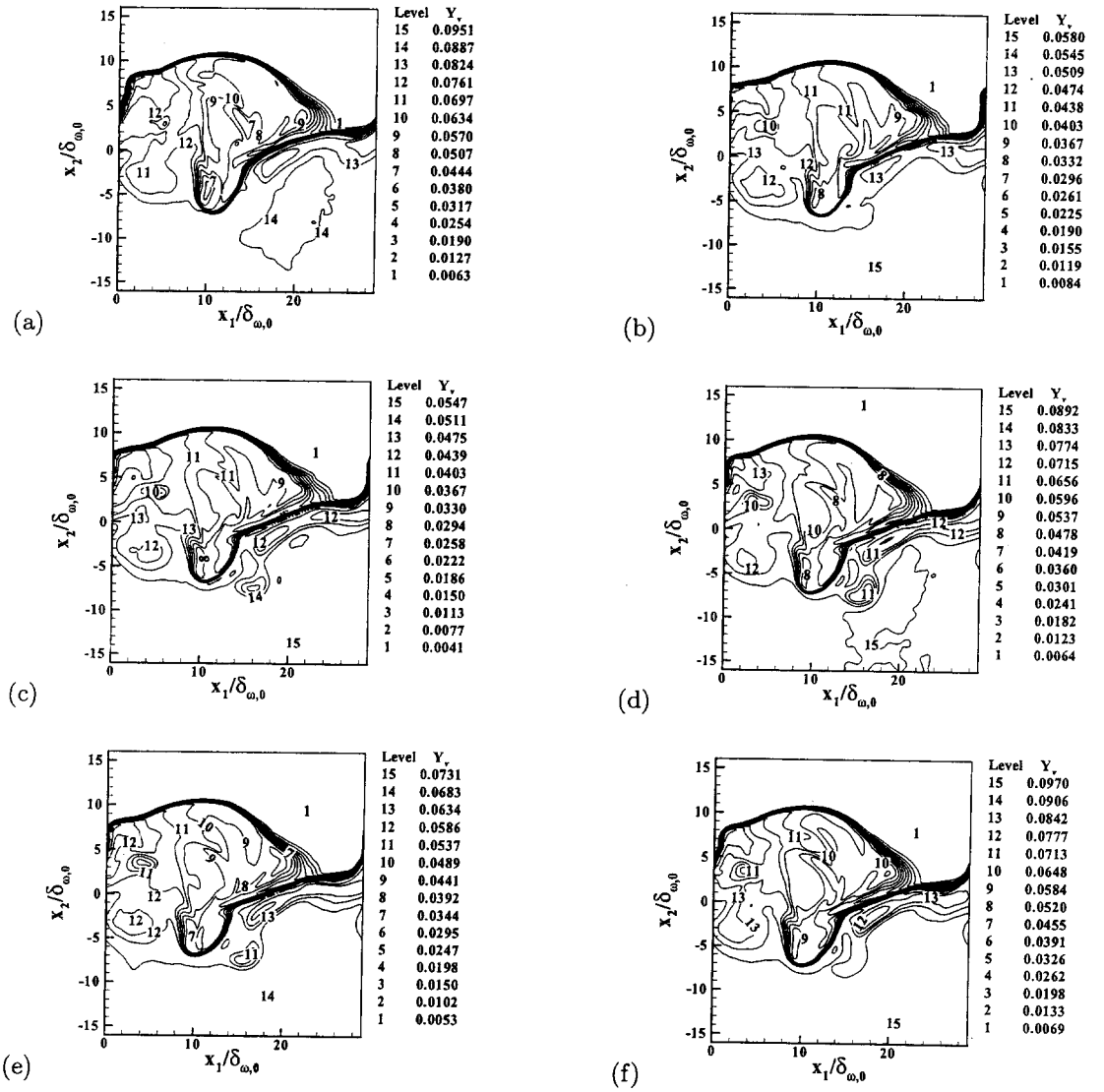

Fig. 6 Contour plots of the vapor mass fraction in the between-the-braid plane at $t^* = 95$. SCdec375 (a), MCdie375x (b), MCdie375 (c), MCdie425 (d), MCdie400 (e), and MCjetA400 (f).

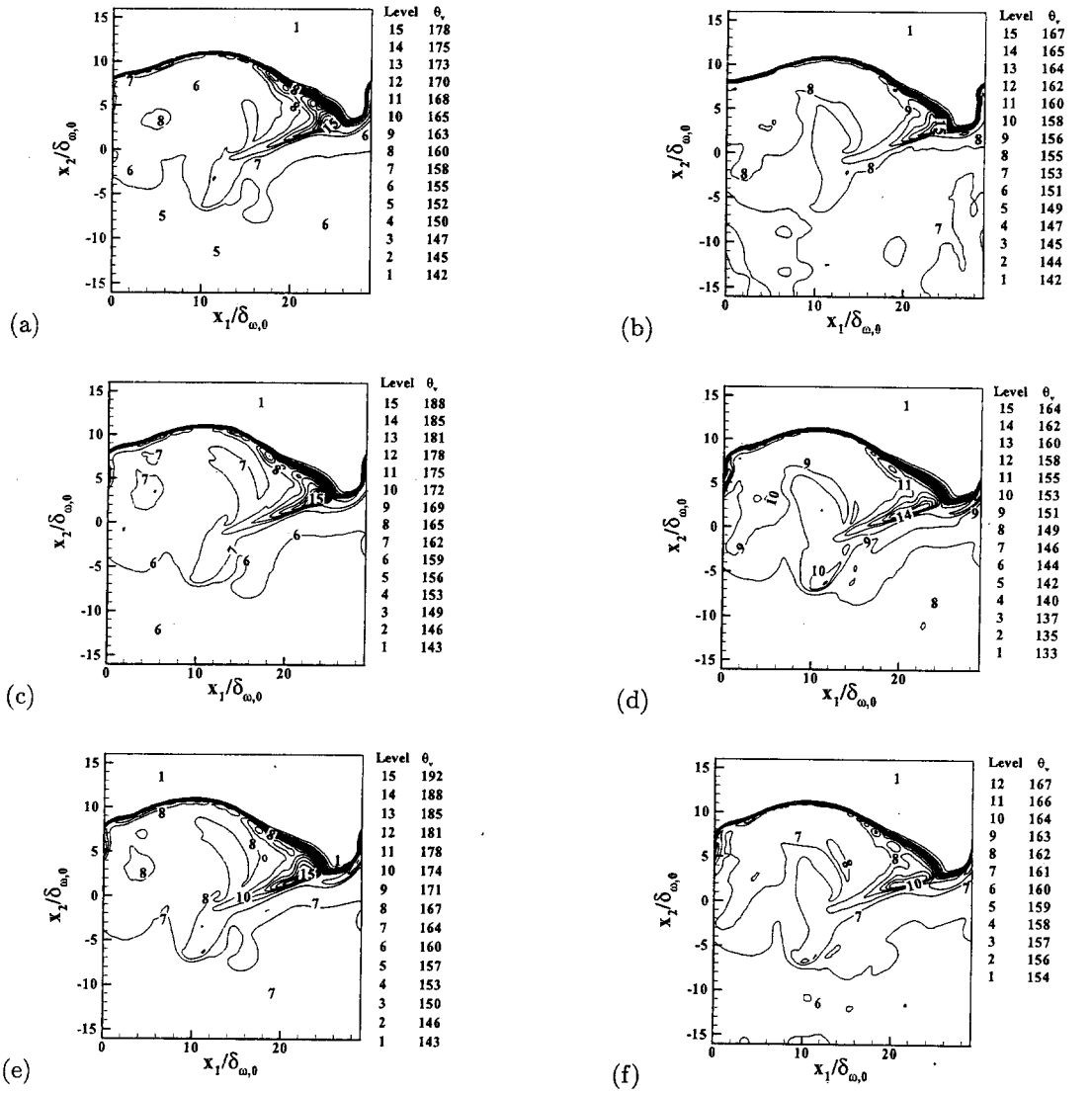

Fig. 7 Contour plots of the vapor mean molar weight (kg/kmole) in the between-the-braid plane at $t^* = 95$. MCdie375 (a), MCdie375x (b), MCdie400 (c), MCjetA400 (d), MCdie425 (e), and MCrp1400 (f).

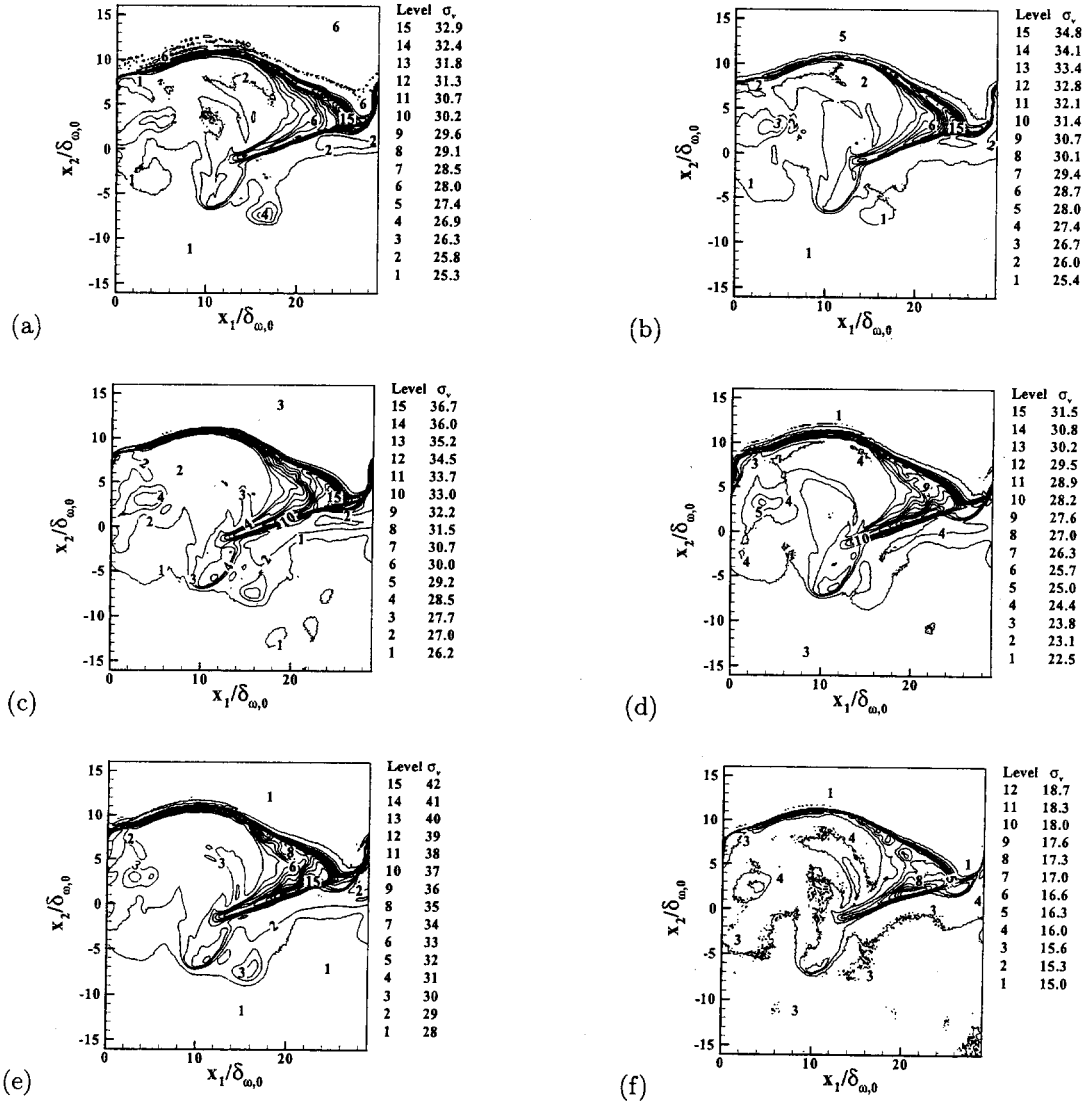

Fig. 8 Contour plots of the vapor composition standard deviation (kg/kmole) in the between-the-braid plane at $t^* = 95$. MCdie375 (a), MCdie375x (b), MCdie400 (c), MCjetA400 (d), MCdie425 (e), and MCrp1400 (f).

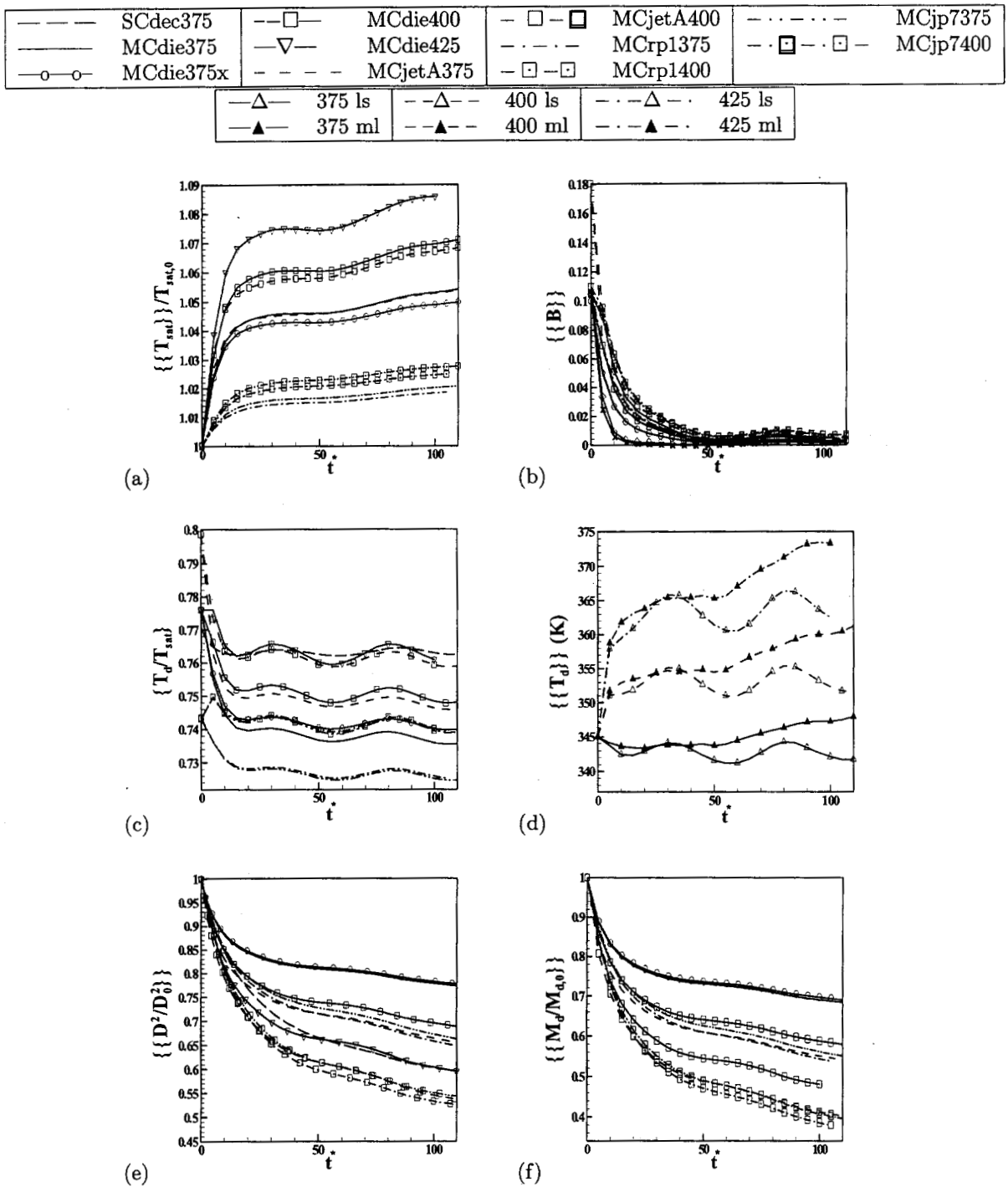

Fig. 9 Timewise evolution of the normalized saturation temperature (a), the ensemble average transfer number (b), the ensemble average drop temperature over the saturation temperature (c), the ensemble average drop temperature in the lower stream (ls) and the mixing layer (ml) (d), the ensemble average of the normalized drop diameter square (e), and the ensemble average normalized drop mass (f).The legend for figures (a,b,c,e,f) is displayed in the top box above the figures and the legend for figure (d) is displayed in the second to the top box.

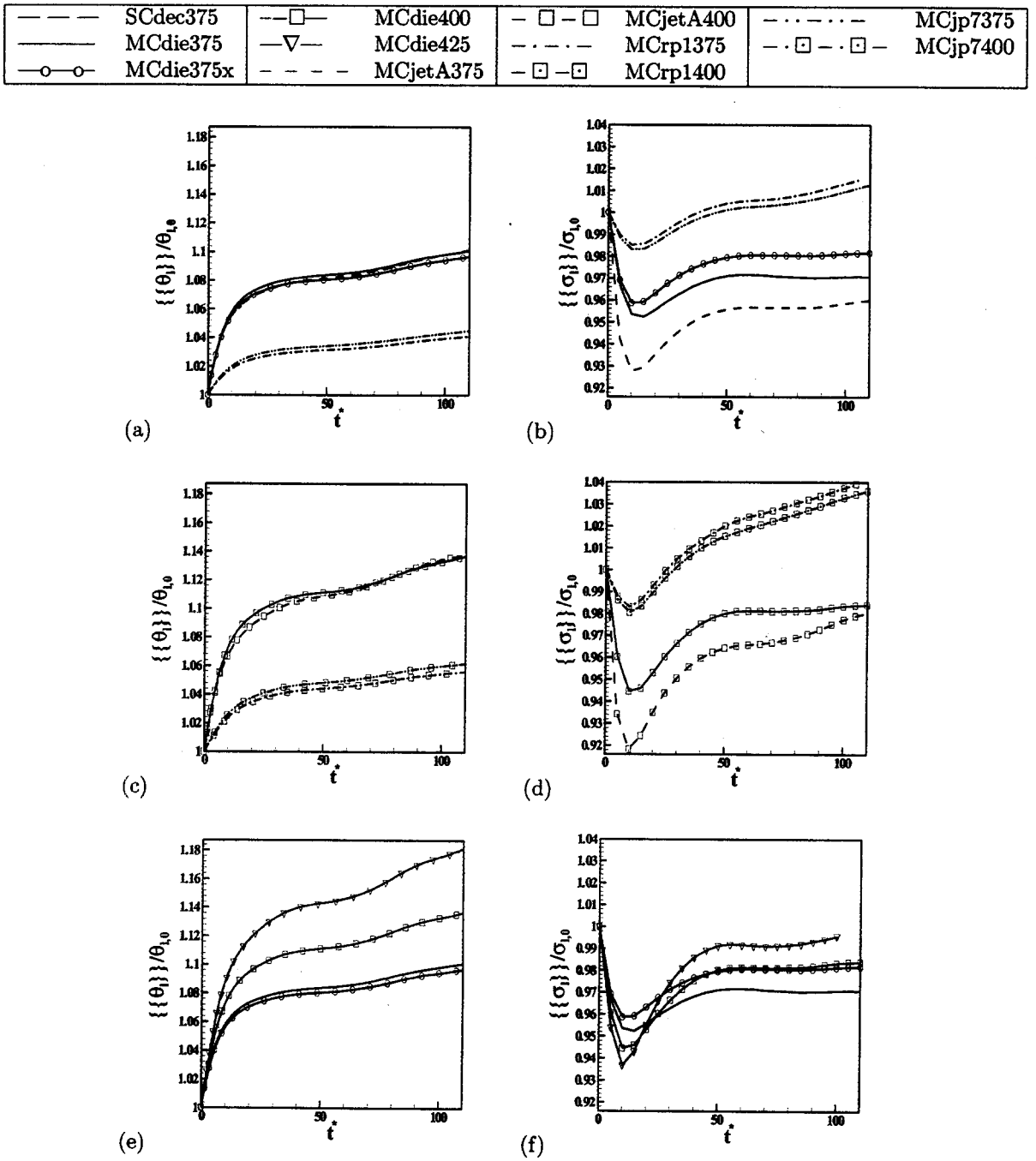

Fig. 10 Timewise evolution of the normalized ensemble average liquid mean molar weight (a,c,e) and standard deviation (b,d,f).

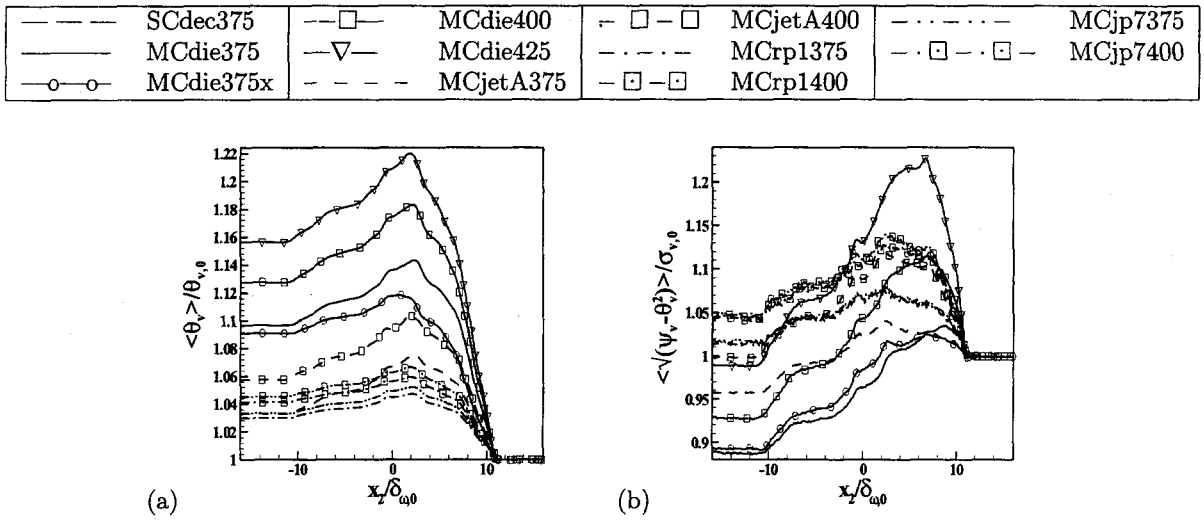

Fig. 11 Homogeneous-plane averages at $t^* = 95$ of the normalized vapor mean molar weight (a) and the normalized standard deviation (b).